Benchmark computations for 3D two-phase flows: A coupled lattice Boltzmann-level set study

Mohammad Amin Safi[a,b*], Stefan Turek[a], Nikolaos Prasianakis[c]
[*]Corresponding author; seyed.safi@psi.ch

[a]Paul Scherrer Institute, Energy and Environment Division, Combustion Research Laboratory, CH-5232 Villigen-PSI, Switzerland
[b]Institute of Applied Mathematics (LSIII), TU Dortmund, Vogelpothsweg 87, D-44221 Dortmund, Germany
[c]Paul Scherrer Institute, Nuclear Energy and Safety Division, Waste Management Laboratory, CH-5232 Villigen-PSI, Switzerland

Abstract

Following our previous work on the application of the diffuse interface coupled lattice Boltzmann-level set (LB-LS) approach to benchmark computations for 2D rising bubble simulations, this paper investigates the performance of the coupled scheme in 3D two-phase flows. In particular, the use of different lattice stencils, e. g., D3Q15, D3Q19 and D3Q27 is studied and the results for 3D rising bubble simulations are compared with regards to isotropy and accuracy against those obtained by finite element and finite difference solutions of the Navier-Stokes equations. It is shown that the method can eventually recover the benchmark solutions, provided that the interface region is aptly refined by the underlying lattice. Following the benchmark simulations, the application of the method in solving other numerically subtle problems, e. g., binary droplet collision and droplet splashing on wet surface under high Re and We numbers is presented. Moreover, efficient implementations on general purpose GPUs are pursued, where the computations are adaptively refined around the critical parts of the flow. As a result, the computational cost and the required memory are shown to be at least 50% lower than similar two-LBE solutions for 3D two-phase flow simulations.

Keywords 3D rising bubble; Lattice Boltzmann method; Level set method; Droplet splashing; Binary droplet collision; GPGPU implementation

1 Introduction

The application of the coupled lattice Boltzmann-level set scheme for two-phase flows to 2D benchmark simulations was discussed previously in the works of Safi and Turek in [23], coupling a one-fluid lattice Bolztmann equation (LBE) with signed distance level set equation (LSE) as a sharp interface method. This methodology was shown to be prone to unphysical velocities caused by weak pressure approximation in the one-fluid LBE. The alternative pressure evolution LBE is more robust at large pressure gradients but breaks down in calculating non-ideal part of the pressure if a sharp interface method is used. In the later work of Safi and Turek [22] the pressure evolution LBE was thus coupled with a phase field mass conserving LSE. It was shown in [22] that by applying averaged directional differencing to discretize the pressure forcing terms in LBE, one can use the continuum surface force (CSE) form of the surface tension forces and obtain stable and accurate solutions at high density and viscosity ratios as examined for 2D rising bubble benchmarks. In fact,

such a methodology also offers an alternative to the two-LBE schemes as in the pressure evolution scheme of Lee et. al [16] or the free-energy implementation of Banari et. al. [5] which require to save and process data for a second group of distribution functions which are used to solve the LBE for the order parameter. Considering the fact that diffuse interface LB-based solutions often require high lattice resolutions and 3D lattice stencils need 15-27 populations, pursuing a two-LBE strategy for 3D flows ends up in extremely large amounts of computational time and memory. The memory issue is even more demanding for parallel implementations on general purpose GPUs (GPGPU) where memory resources per GPGPU are scarce. This in turn puts severe restrictions on the resolution as well as the size of the problem and could potentially limit the applicability of such schemes.

On the other hand, to the knowledge of the authors, 3D simulations of two-phase flows have always been validated against experimental results in the so-called picture norms as in [3], [7], [17], where correspondence between the input setting of the numerical simulation to the setup data in the laboratory is often very hard, if not impossible. Consequently, from the users point of view, it is yet unclear how close the obtained numerical results could get to the direct numerical simulation of the two-phase Navier-Stokes equations (NSE), especially in situations where the exact extent and rate of interface deformation are of paramount importance.

In this paper, we extend the methodology of diffuse coupled LB-LS to 3D flows, where the recent results obtained by finite element solutions of NSE for 3D rising bubbles [28] will be used as reference to examine the accuracy of the coupled scheme for different test cases. The benchmarking also enables us to investigate the effect of using various discrete velocity stencils in LB method. Having established the accuracy in 3D, the numerical robustness of the coupled LB-LS scheme will be examined for non-benchmark flows involving strong deformations, e. g., droplet splashing on surface and binary droplet collision under high Re and We numbers. On the computational side, adaptive techniques for parallel GPGPU implementations are discussed so as to effectively manage computational cost of 3D simulations.

The paper is organized as follows. The coupled LB-LS scheme will be shortly explained in section 2. Benchmark test cases for 3D rising bubbles will be introduced in section 3, including a brief review of the numerical procedure used in the reference computations. The section eventually presents the numerical results for the rising bubble problems. Application of the scheme to other numerically and physically interesting two-phase flows will be the subject of section 5. Section 6 briefly describes the GPGPU implementation and the obtained computational performances. The paper will be closed with conclusions and discussions in section 7.

2 Coupled LB-LS scheme

The LBE for the evolution of density distribution functions f_α along discrete velocity directions $\alpha = 0, ..., n$ with BGK approximation for collision reads

$$\frac{\partial f}{\partial t} + c_\alpha \cdot \nabla f = -\mathbf{\Lambda}(f_\alpha(x,t) - f_\alpha^{eq}(x,t)) - \frac{(c_\alpha - \mathbf{u}) \cdot \mathbf{F}}{c_s^2} f^{eq}(x,t) \tag{1}$$

where $\mathbf{F}$ is the forcing term and f_α^{eq} is the equilibrium distribution

$$f_\alpha^{eq}(\rho, \mathbf{u}) = w_\alpha \rho \left[1 + \frac{c_\alpha \cdot \mathbf{u}}{c_s^2} + \frac{[c_\alpha \cdot \mathbf{u}]^2}{2c_s^4} + \frac{[\mathbf{u} \cdot \mathbf{u}]}{2c_s^2} \right] \tag{2}$$

with w_α being the weight factors for each discrete direction. The general relaxation matrix $\mathbf{\Lambda}$ could be replaced by $1/\tau$ for a single relaxation time (SRT) collision, while in a multiple relaxation time (MRT) collision it takes the following form

$$\mathbf{\Lambda} = \mathbf{M}^{-1}\hat{\mathbf{\Lambda}}\mathbf{M} - 2\mathbf{I} \tag{3}$$

where $\mathbf{M}$ constructs n hydrodynamic moments from f_αs and $\hat{\mathbf{\Lambda}} = Diag\{s_1, ..., s_n\}$ is the diagonal relaxation matrix so as to let different hydrodynamic moments relax to their corresponding equilibrium states via individual relaxation rates. The force term $\mathbf{F}$ arising from two-phase effects in the LB framework is

$$\mathbf{F} = \nabla(\rho c_s^2 - p) - \mathbf{F}_s + \mathbf{G}. \tag{4}$$

The first term in equation 4 is the gradient of the non-ideal part of the pressure p, where ρ is the density and $c_s = 1/\sqrt{3}$ is the lattice speed of sound. $\mathbf{G}$ is a volume force, e. g. gravity. The second term, is the diffuse CSF form of surface tension force

$$\mathbf{F}_s = \sigma\kappa\mathbf{n}\delta_\varepsilon \tag{5}$$

where σ is the surface tension coefficient, $\mathbf{n}$ is the normal to the interface, κ is the interface curvature. The delta function δ_ε is used to apply the force in a diffuse manner over a thickness ε around the interface. In addition, one may define the continuous phase-field scalar ψ to denote the interface location as

$$\psi = \begin{cases} 1 & if \quad \mathbf{x} \in \Omega_1 \\ 0.5 & if \quad \mathbf{x} \in \Gamma \\ 0 & if \quad \mathbf{x} \in \Omega_2 \end{cases} \tag{6}$$

where Ω_1 and Ω_2 point to phase 1 and 2, respectively and Γ is the location of the interface. Note that ψ decays continuously from 1 to 0 while crossing the interface. Moreover, based on the phase-field definition of ψ one may deduce $\nabla\rho = \nabla\psi(\rho_1 - \rho_2)$. The definition also helps constructing interface properties as functions of ψ

$$\mathbf{n}(\psi) = \frac{\nabla\psi}{|\nabla\psi|} \quad , \quad \kappa(\psi) = \nabla\cdot\mathbf{n} = \nabla\cdot\left(\frac{\nabla\psi}{|\nabla\psi|}\right) \quad , \quad \delta_\varepsilon(\psi) = |\nabla\psi|. \tag{7}$$

In order to rectify the destructive numerical effect of the $\nabla(p - \rho c_s^2)$ at high density ratios, He et. al [11] proposed to use pressure distribution functions g_α

$$g_\alpha = f_\alpha c_s^2 + (p - \rho c_s^2)w_\alpha, \tag{8}$$

and thus solve the pressure evolution LBE by taking the total derivative of g_α as

$$\frac{Dg_\alpha}{Dt} = \frac{\partial g_\alpha}{\partial t} + c_\alpha.\nabla g_\alpha = \mathbf{\Lambda}(g_\alpha - g_\alpha^{eq}) + (c_\alpha - \mathbf{u})\cdot\left[\nabla\varphi(\Gamma_\alpha(\mathbf{u}) - w_\alpha) + (\mathbf{F}_s + \mathbf{G})\Gamma_\alpha(\mathbf{u})\right]. \tag{9}$$

Details for time integration and spatial discretization of equation (9) could be found in [16] and [22]. In essence, by applying trapezoidal rule for time integration and using average and central directional differencings, one obtains

$$\begin{aligned} \bar{g}_k(x + c_\alpha\Delta t, t + \Delta t) =& \bar{g}_k(x,t) - (\Lambda + 2\mathbf{I})(\bar{g}_\alpha(x,t) - \bar{g}_\alpha^{eq}(x,t)) + \\ & (c_\alpha - \mathbf{u})\cdot\left[(\sigma\nabla^c\cdot(\frac{\nabla^c\psi}{|\nabla^c\psi|})\nabla^c\psi + \mathbf{G})\Gamma_\alpha(\mathbf{u})\right]\Big|_{(x,t)} + \\ & (c_\alpha - \mathbf{u})\cdot\left[\Delta\rho c_s^2(\Gamma_\alpha(\mathbf{u}) - w_\alpha)\nabla^{ave}\psi\right]\Big|_{(x,t)} \end{aligned} \tag{10}$$

where the transformed distributions $\bar{g}_\alpha$ and $\bar{g}_\alpha^{eq}$ are defined as

$$\begin{aligned}\bar{g}_\alpha = &\quad g_\alpha + \frac{\Lambda}{2}(\bar{g}_\alpha - \bar{g}_\alpha^{eq}) - \frac{1}{2}(c_\alpha - \mathbf{u}) \cdot [\nabla\varphi(\Gamma_\alpha(\mathbf{u}) - w_\alpha) + (\mathbf{F}_s + \mathbf{G})\Gamma_\alpha(\mathbf{u})] \\ \bar{g}_\alpha^{eq} = &\quad g_\alpha^{eq} - \frac{1}{2}(c_\alpha - \mathbf{u}) \cdot [\nabla\varphi(\Gamma_\alpha(\mathbf{u}) - w_\alpha) + (\mathbf{F}_s + \mathbf{G})\Gamma_\alpha(\mathbf{u})]\,.\end{aligned} \tag{11}$$

Finally, the pressure and velocity of the flow are recovered as moments of new distribution functions $\bar{g}_\alpha$

$$p = \sum_\alpha \bar{g}_\alpha + \frac{c_s^2 \Delta\rho}{2}\mathbf{u} \cdot \nabla^c\psi \tag{12}$$

$$\rho\mathbf{u} = \frac{1}{c_s^2}\sum_\alpha \bar{g}_\alpha + \frac{1}{2}(\sigma\nabla^c \cdot (\frac{\nabla^c\psi}{|\nabla^c\psi|})\nabla^c\psi + \mathbf{G}). \tag{13}$$

In order to capture the interface, the LBE in equation (10) is coupled with a mass conserving LSE proposed by Olsson and Kreiss [20] so as to solve the evolution of the scalar field ψ as it moves with the flow velocity $\mathbf{u}$

$$\partial_t\psi + \mathbf{u} \cdot \nabla\psi = -\nabla \cdot (\psi(1-\psi)\mathbf{n}) + \eta\nabla^2\psi. \tag{14}$$

Note that the initial profile of ψ is obtained by iteratively solving equation (14) to reach steady state. The parameter η controls the thickness and could be chosen as

$$\eta = \frac{h^\beta}{2} \tag{15}$$

where h is the spatial resolution and the exponent β is chosen to be close to 1 so as to control the interface thickness and has a subsequent effect on the quality of the interface capturing as well as the overall mass conservation. We use second order Runge-Kutta for time integration of equation (14) and the fifth order WENO for its convective term. The terms on the righ hand side are then treated explicitly and discretized in space using central differencing. Since the time scales enforced by the solution of the LBE are quite small, such a discretization for these non-linear terms will not introduce any noticeable numerical deficiency.

2.1 MRT collision for 3D LBM

In order to reinforce the stability of the LBE solver at low viscosities and high Re numbers, the present implementation employs a MRT collision for 3D implementations through replacing $\mathbf{\Lambda} + 2\mathbf{I}$ with $\mathbf{M}^{-1}\hat{\mathbf{\Lambda}}\mathbf{M}$ in equation (10). An extensive description of the principal moments for D3Q15 and D3Q19 stencils is done in [9] and [18]. For the D3Q27 stencil, the MRT methodology given in [24] for turbulent flows in adopted here. The general choice of the relaxation times for all stencils would be analogous to those outlined in our previous 2D implementations [23] and [22] which requires under-relaxing the energy moments so as to eliminate the initial fluctuations in the velocity of a rising bubble. A detailed discussion is beyond the scope of this paper and could be found in [21].

3 3D rising bubble benchmarks

Inspired by the 2D work in [12], the rising bubble benchmarks were extended for 3D effects in the works of Turek et. al [28] and Adelsberger et al. [2]. The problem consists of an initially stagnant bubble of radius $r_0 = 0.25$ and located at $(x, y, z) = (0.5, 0.5, 0.5)$ which starts to rise due to buoyancy through the liquid in a 3D rectangular domain of size $1 \times 1 \times 2$ as depicted in figure 1. The buoyancy force is

$$\mathbf{G} = (\rho_1 - \rho_2)\mathbf{g} \tag{16}$$

where $\mathbf{g} = (0, -g)$ is the gravity and ρ_1 and ρ_2 are the liquid and gas densities, respectively. Note that $\mathbf{G}$ is only exerted as a net force to the gas inside the bubble. No-slip boundary conditions are applied to all boundaries including the side walls where the second order half-way bounceback rule is imposed. Moreover, due to the symmetry of the problem in the horizontal plane, only 1/4 of the problem is solved to save computational cost and memory, where the center of the bubble will be located at $(x, y, z) = (0, 0, 0.5)$ and the symmetry boundary condition is applied to $x = 0$ and $y = 0$ planes.

Two sets of input data are then used to define two test cases as summarized in table 1. The hydrodynamics in both cases are governed by the non-dimensional Re and Eo numbers

$$Re = \frac{\rho_1 \sqrt{g}(2r_0)^{3/2}}{\mu_1} \tag{17}$$

$$Eo = \frac{4\rho_1 g(r_0)^2}{\sigma}. \tag{18}$$

The LB code uses the same values of density and viscosity as in table 1, while g_{lb} and σ_{lb} are obtained based on equations 17 and 18 using LB units for r_0. In order to preserve consistency with the macroscopic time measurement in [28] and [2], the following equation is used to calculate the macroscopic time based on LB iterations t_{lb}

$$T = t_{lb}\sqrt{\frac{g_{lb}}{gL_0}}$$

where $L_0 = 1/h$ is the characteristic length in lattice units, with h being the physical resolution. For both test cases, simulations are carried until $T = 3$. Analogous to the 2D problems in [22], the first test case, referred to as TC1, is a low density ratio system where the the relatively small value of Eo number tends to keep the bubble in a round shape as it rises. In the second test case, however, the density and viscosity ratios are increased to 1000 and 100, respectively, and the Eo number is increased to 125. The latter particularly allows for large deformation rates implied by weak surface tension forces.

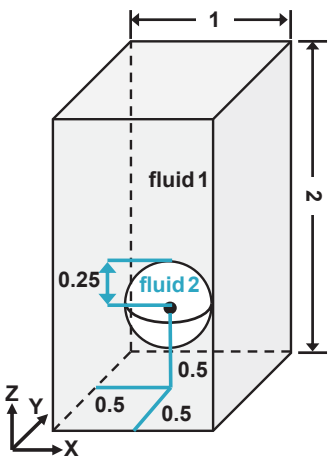

Fig. 1: Illustration of the rising bubble problems in the 3D problem.

Table 1: Physical parameters and dimensionless numbers for TC1 and TC2 rising bubble problems.

Test case	ρ_1	ρ_2	μ_1	μ_2	g	σ	Re	Eo	ρ_1/ρ_2	μ_1/μ_2
TC1	1000	100	10	1	0.98	24.5	35	10	10	10
TC2	1000	1	10	0.1	0.98	1.96	35	125	1000	100

In order to quantify the dynamics of the bubble during its course of rise, a number of benchmark quantities are defined and used throughout this paper. To track the bubble position during the rise process, the bubble centroid coordinate (x_c, y_c) is computed as

$$X_c = (x_c, y_c) = \frac{\int_{\Omega_2} \mathbf{x} dx}{\int_{\Omega_2} 1 dx}$$

where Ω_2 encompasses all the lattice points inside the bubble. The degree of roundness of a 3D bubble can be measured based on the sphericity parameter defined in [29] as

$$\Psi = \frac{A_a}{A_b} = \frac{\text{area of volume-equivalent sphere}}{\text{area of bubble}} = \frac{\pi^{1/3}(6V_b)^{2/3}}{A_b}.$$

The mean velocity with which the bubble is rising is defined as

$$\mathbf{U_c} = \frac{\int_{\Omega_2} \mathbf{u}\ dx}{\int_{\Omega_2} 1\ dx}.$$

The last quantity is the bubble size which describes the maximum extension (diameter) of the bubble in the main coordinate directions which together with the bubble circularity and sphericity further specifies the deformation state of the bubble. It is calculated as

$$d_i = max_{p,q \in \Omega_2} |p_i - q_i|, \qquad i = x, y, z.$$

where p and q are any two arbitrary points which belong to the bubble.

3.1 Review of the numerical tools

The numerical simulations performed by the current coupled LB-LS scheme, will be compared against two sets of solutions of the two-phase flows. The first group, also considered here as the reference solution, is the one obtained by the finite element FeatFlow package [1] designed for solving incompressible NSE. The two-phase solver is based on coupling the NSE with the signed distance-based LSE. Space discretization in the 3D code makes use of Q_2 elements for velocity and discontinuous P_1 elements for pressure. Besides Q_2 elements are used for solving the LS equation. Time integration is carried out via a Crank-Nicolson scheme which is used in the 3D implementations. A full description of the solvers could be found in [28].

Another two-phase flow solver for 3D simulations is the finite difference-based NaSt3D code [2]. It solves the Navier-Stokes equation on an equidistant grid. Chorin's projection method is used to decouple velocity and pressure fields, where a second order explicit Adams-Bashforth scheme is employed to solve the velocity while the pressure is recovered via solving the Poisson equation. The interface is captured through a signed distance LS function and the bubble mass is corrected using the local correction scheme of Sussman and Fatemi [25].

4 Numerical Results

The D3Q19 stencil is adopted as the default discrete velocity stencil which is known to posses a higher isotropy than the D3Q15 stencil and imposes only a moderate increase in the computational workload. The choice will be verified later on through detailed comparisons of the results obtained by D3Q15, D3Q19 and D3Q27 velocity models against the benchmark data. Yet, regardless of the type of the lattice stencil in use and considering the 5.7 GB memory available on Kepler 20x GPGPU used for the present simulations, the maximum lattice resolution is selected to be $1/h = 256$ corresponding to a grid of $128 \times 128 \times 512$ which occupies 3.9 GB of memory for 1/4 of the problem using the D3Q19 stencil.

4.1 Test case 1

The evolution of the 3D bubble interface in TC1 up to $T = 3$ is presented in figure 2 on a lattice of $1/h = 256$ and the reference shapes obtained by FeatFlow on a grid of $1/h = 128$. The bubble develops into an ellipsoidal shape as predicted in the bubble shape regime map of Clift et. al [8]. However, compared to the 2D cases in [22], it preserves its initial sphericity to a higher degree such that almost no deformation occurs after $T = 2.0$.

The convergence of the interface shape is also studied in figure 3, followed by more detailed comparisons between the bubble quantities obtained by LBM NaSt3D, and the reference values of FeatFlow in figures 4 to 7. For the low deformation rate of TC1, the present maximum lattice resolution seems to be sufficient to repeat the reference data by FeatFlow. For the rise velocity, the discrepancies grow around the peak values although the difference between the LBM data on $1/h = 256$ and that of FeatFlow amounts to less than 0.5%. A similar behavior is observed for the interface-related sphericity and diameter values around $T = 1.5$ where the overall convergence trend is towards the reference curves.

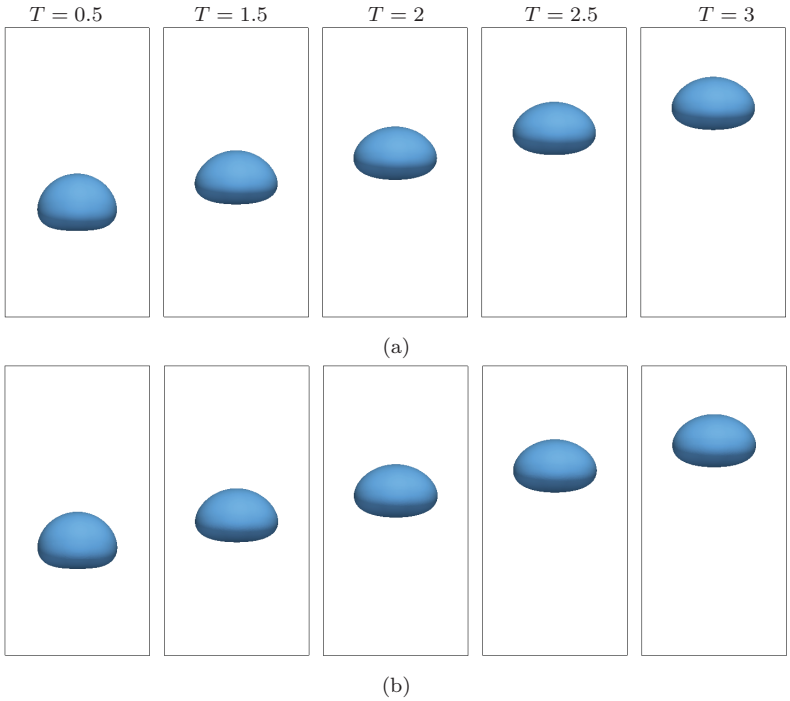

Fig. 2: Time evolution of the bubble in 3D problem of TC1 using (a) coupled LB-levelset, (b) FeatFlow.

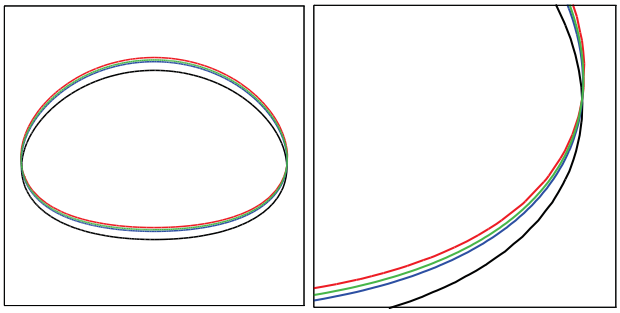

Fig. 3: Terminal shape of bubble at $T = 3$ for 3D problem of TC1 with enlarged view (right), on different lattice resolutions; $1/h = 96$ (black), $1/h = 192$ (blue), $1/h = 256$ (green) and FeatFlow on $1/h = 128$ (red).

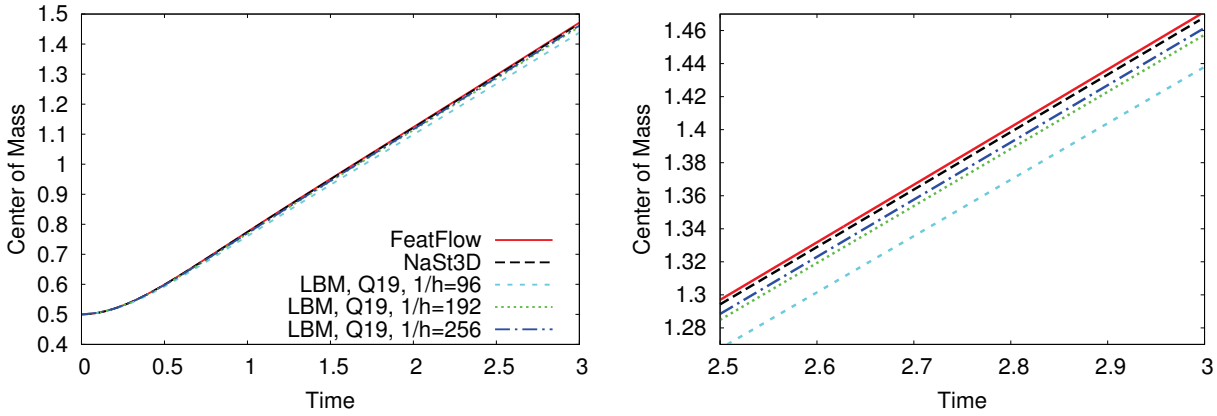

Fig. 4: Time evolution of center of mass for 3D rising bubble TC1 (left), and enlarged view (right).

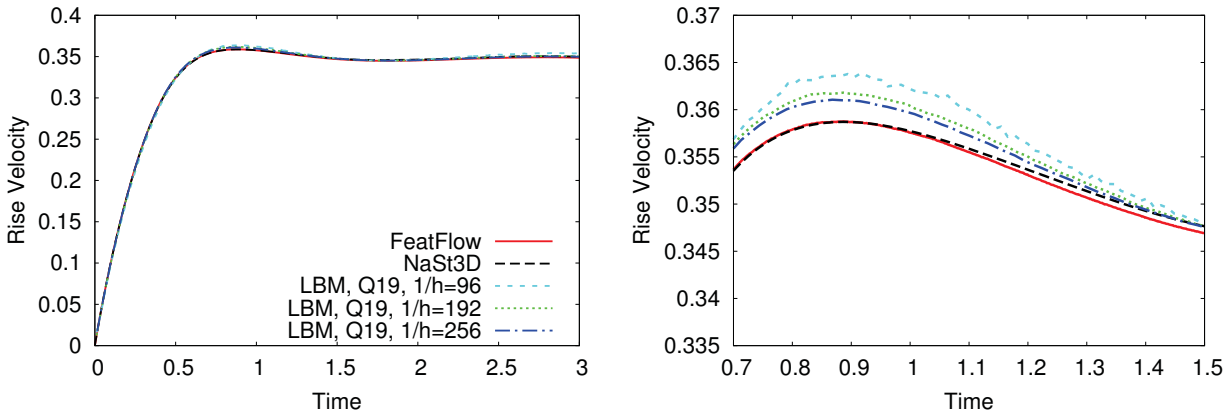

Fig. 5: Time evolution of rise velocity for 3D rising bubble TC1 (left), and enlarged view (right).

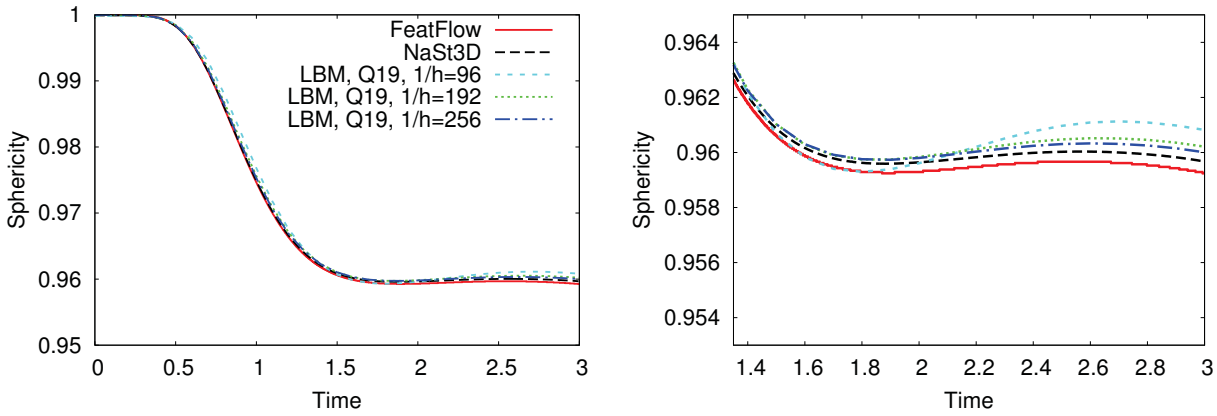

Fig. 6: Time evolution of circularity for 3D rising bubble TC1 (left), and enlarged view (right).

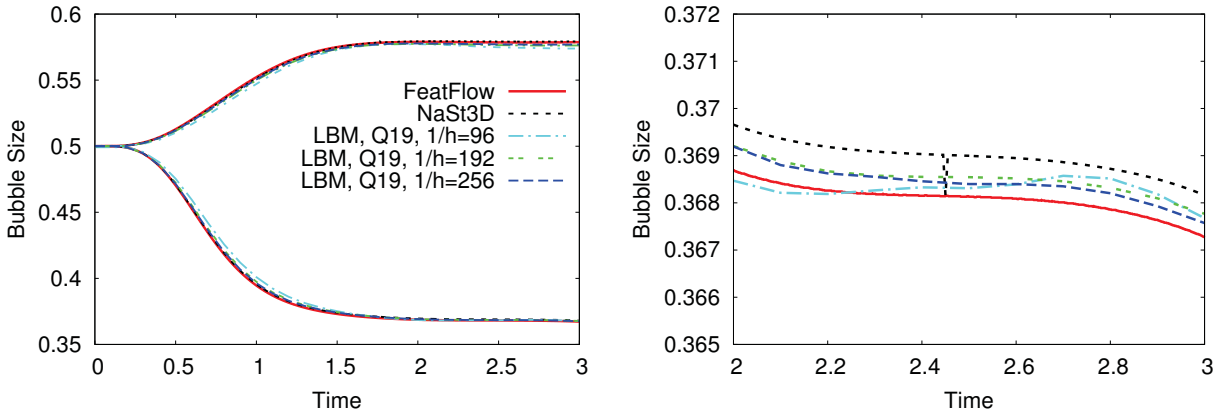

Fig. 7: Time evolution of diameters in horizontal and vertical directions for 3D rising bubble TC1 (left), and enlarged view (right).

4.2 Test case 2

The 3D bubble shown in figure 8(a) experiences strong deformations provoked by the weaker surface tension effects due to a relatively large Eo number. The bubble first deforms into a dimpled cap and then proceeds to extend the edges so that the eventual cusp-shaped bubble is formed as predicted in [8]. Yet again, the diffuse nature of the present coupled scheme prevents the bubble to develop sharp edges, e. g., those predicted by Featflow in figure 8(b). Nevertheless, the picture norm admits the close relevance of the overall evolution trend in both schemes. Examining the convergence trend in the interface shape in figure 9 shows that LBM may eventually converge to the sharp interface solution of the two-phase Navier-Stokes equations, provided that the lattice would be sufficiently refined, as in the 2D counterpart of TC2 in [22] where a resolution of $1/h = 640$ was used to approach the sharp interface results.

The convergence of the bubble quantities together with the NaSt3D data and the reference data of FeatFlow are collected in figures 10 to 13. The agreement between the rise velocities keeps favorably up to $T = 1.5$ which confirms a decent performance of the D3Q19 discrete model in recovering the correct pressure and velocity fields under high density and viscosity differences. For $T > 1.5$, as the bubble starts to develop the cusp shape, the phase-field LSM falls behind the sharp LSM, and tries to keep the edges prolonged and

smooth. In terms of bubble quantities, this results in growing deviations from the sharp interface data, which is more clearly seen in the bubble sphericity, diameter and centroid position. Similar to the 2D test case, the sharp interface methods tend to create kinks or teeth-like irregularities on the skirt of the bubble towards $T = 2$ which then makes the solution strongly dependent on the specific parametrization used in different codes.

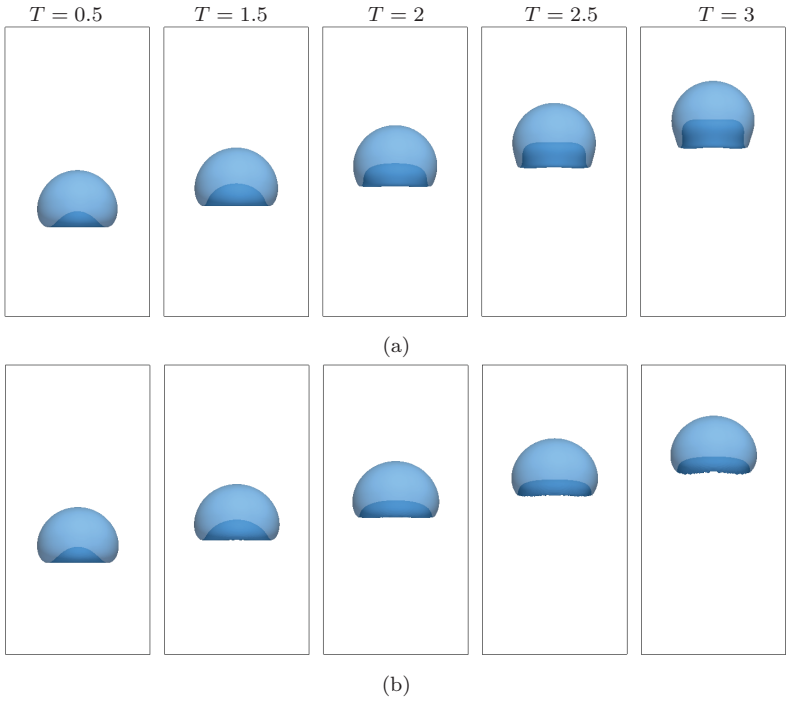

Fig. 8: Time evolution of the bubble in 3D problem of TC2 using (a) coupled LB-levelset (b) FeatFlow. The dark blue regions reflect the interior surface.

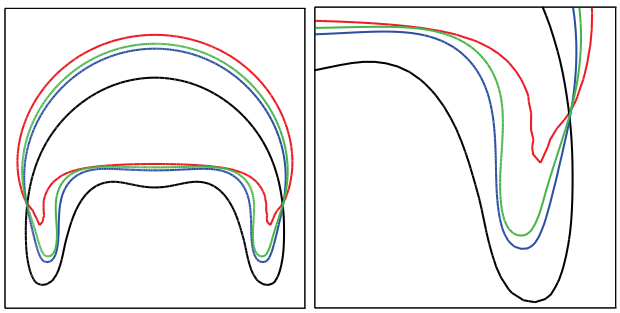

Fig. 9: Terminal shape of bubble at $T = 3$ for 3D problem of TC2 with enlarged view (right), on different lattice resolutions; $1/h = 96$ (black), $1/h = 192$ (blue), $1/h = 256$ (green) and FeatFlow on $1/h = 128$ (red).

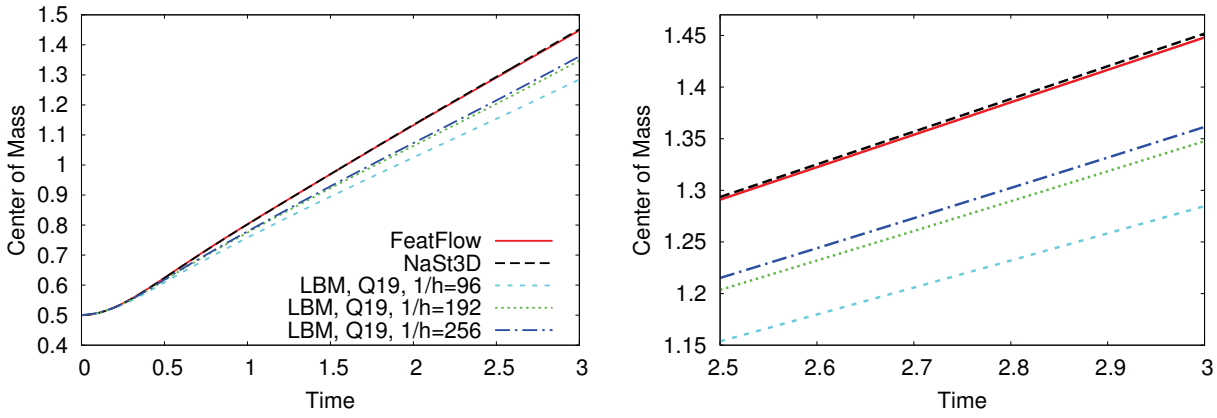

Fig. 10: Time evolution of center of mass for the 3D rising bubble TC2 (left), and enlarged view (right).

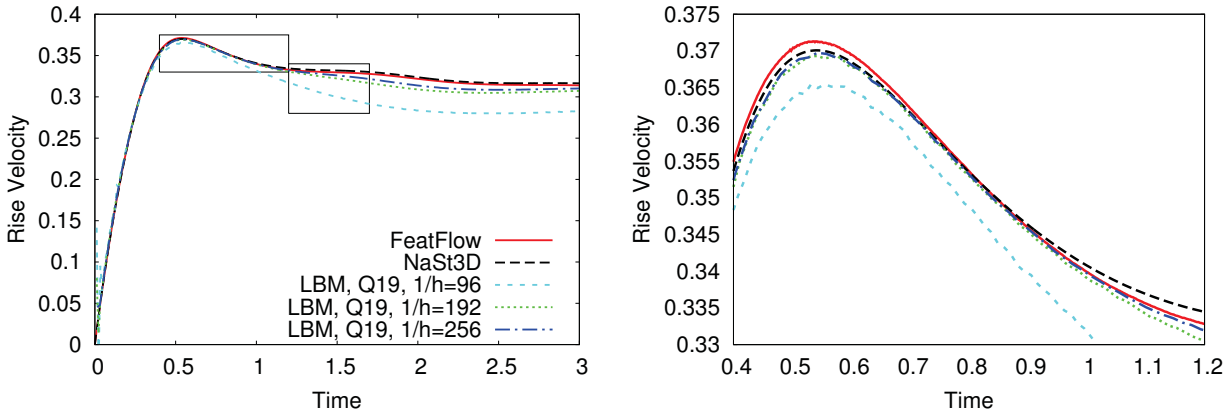

Fig. 11: Time evolution of rise velocity for the 3D rising bubble TC2 (left), and enlarged views (right).

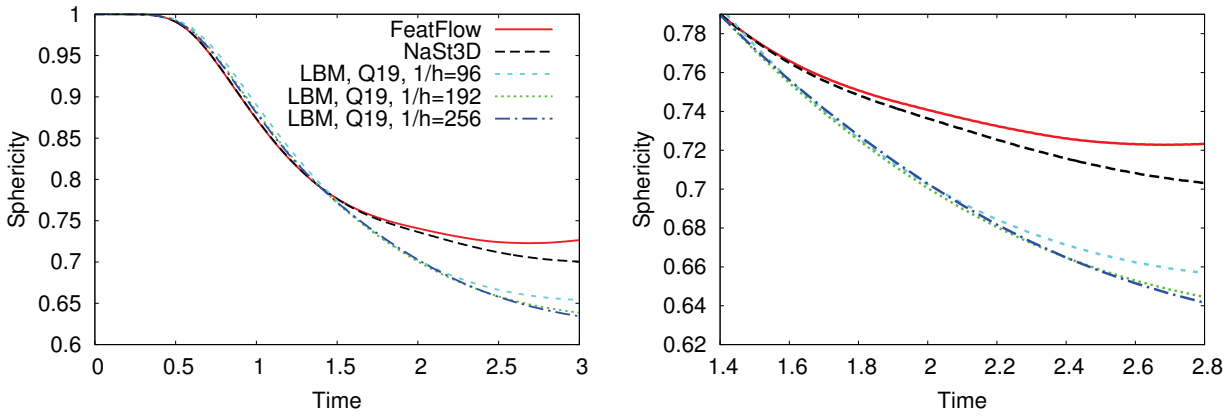

Fig. 12: Time evolution of circularity for the 3D rising bubble TC2 (left), and enlarged view (right).

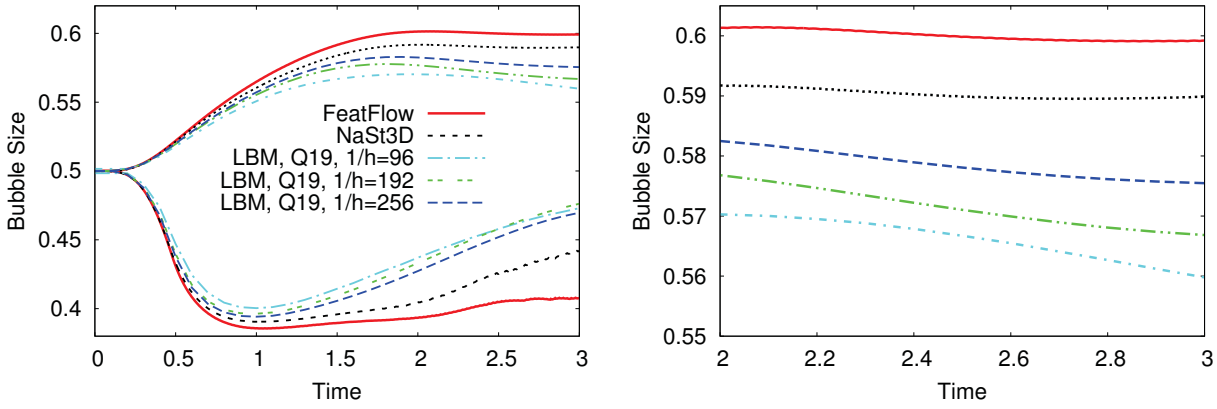

Fig. 13: Time evolution of diameters in horizontal and vertical directions for 3D rising bubble TC2 (left), and enlarged view (right).

4.3 Isotropy and the choice of lattice stencil

The most prominent distinction between discrete velocity stencils, is their associated degrees of isotropy. This property could be best studied through examining the performance of different stencils for TC2, where the presence of four orthogonal walls and the large deformations of the bubble creates a natural anisotropy in the terminal shape of the bubble as shown in figure 15 for the front view and the view from the middle section. The interface lines for the plane perpendicular to the wall ($\theta = 0$) and diagonal plane ($\theta = 45$) are also depicted in figure 16. In the first look, the comparisons unveil the overestimated deformation produced by the D3Q15 model on the diagonal plane. The deviation is caused by the inherent lack of isotropy of the D3Q15 stencil in the diagonal directions on $x - y$, $x - z$, $y - z$ planes (see figure 14). Although one expects to gain the best relevance to the FeatFlow results using the D3Q27 stencil, it is the D3Q19 stencil which exhibits a closer similarity to the FeatFlow shape.

Unlike the observations in the picture norm, the bubble quantities well coincide over time and one could hardly notice significant differences as seen in figures 17 and 18 for bubble velocity and diameter, respectively, on a $1/h = 256$ lattice. For the bubble diameter which is more sensitive to minimal changes in the interface, the D3Q15 stencil shows a more steep return in the vertical diameter up to nearly $d_z = 0.5$ which is also seen by the interface lines in figure 16 where the strong anisotropy yields a longer skirt of the bubble in the diagonal plane.

Finally, the slightly superior accuracy and isotropy of the D3Q19 stencil over the D3Q27 discrete model is still questionable. A likely reason could lie in the choice of the relaxation times in the MRT scheme for different stencils. Exhaustive analysis regarding the optimum choice for the values of the relaxation times is presented in [21]. Therein, the effect of under-relaxation of specific moments has been highlighted. Extending the stencil from 19 to 27 discrete velocities inevitably extends also the range of the hydrodynamic moments that are under consideration. In fact this adds 8 more moments and their respective relaxation times that have to be chosen carefully. The relaxation times of the D3Q27 stencil have been regulated based on the analysis of the D3Q19 stencil and it cannot be excluded that a better set of relaxation parameters could smear out the differences between the two stencils. On the contrary, such an uncertainty does not exist in the case of the D3Q15 stencil, since it is a subset of the D3Q19, and the optimum relaxation times remain exactly same (for the same moments) Nevertheless, the above argument could not be firmly verified as almost all dynamic two-phase LB simulations in the literature are limited to D3Q15 or D3Q19 stencils for computational reasons [26, 6, 30, 31]. Lee and Liu [16] used the D3Q27 discrete model to simulate droplet

impact on dry surfaces. Yet they brought no justification for this choice and provided no comparisons against other discrete models.

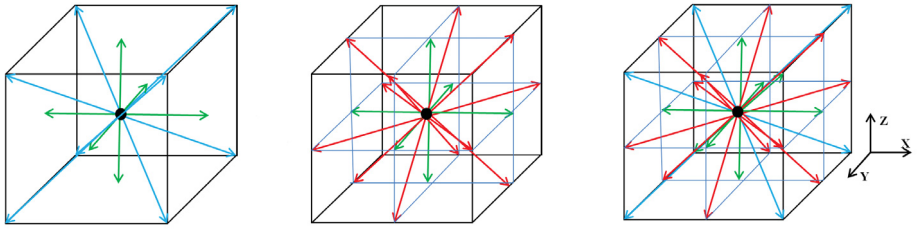

(a) D3Q15 (b) D3Q19 (c) D3Q27

Fig. 14: Different lattice stencils for three dimensional LBM

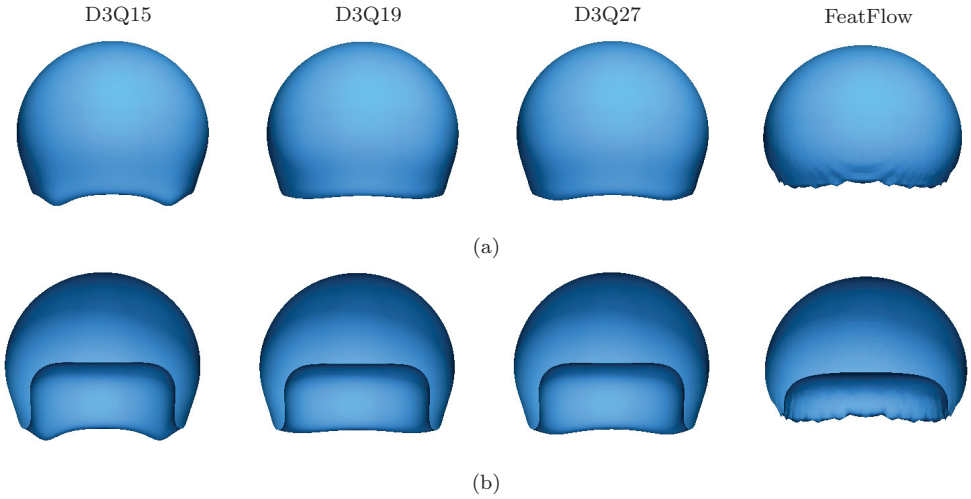

(a)

(b)

Fig. 15: Bubble interface $T = 3.0$ in 3D problem of TC2, (a) exterior view and (b) middle section view.

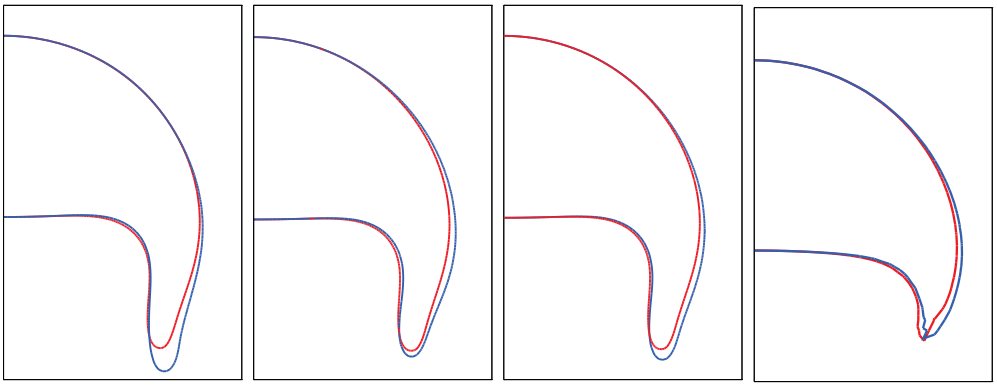

Fig. 16: Bubble interface at $T = 3$ in 3D problem of TC2 for $\theta = 0$ (red) and $\theta = 45$ (blue) planes.

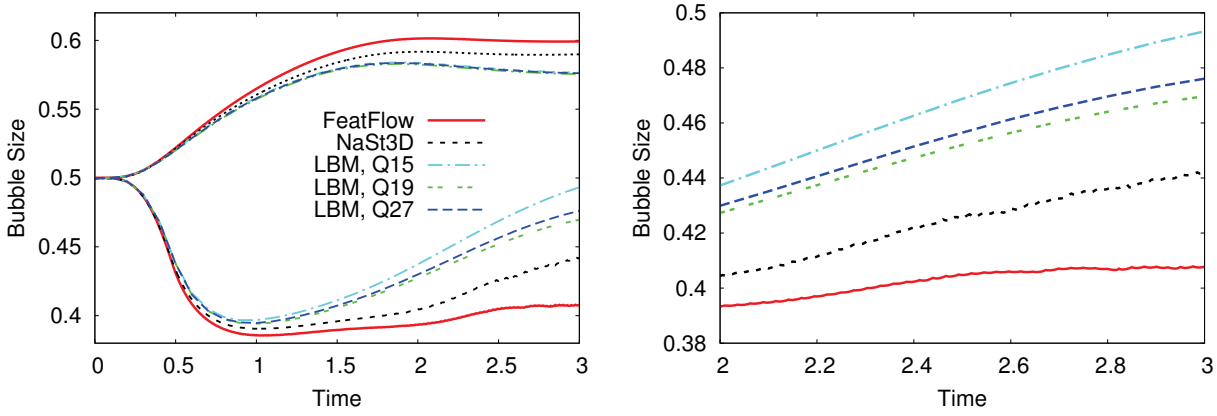

Fig. 17: Time evolution of diameters in horizontal and vertical directions for 3D rising bubble TC2 (left), and enlarged view (right).

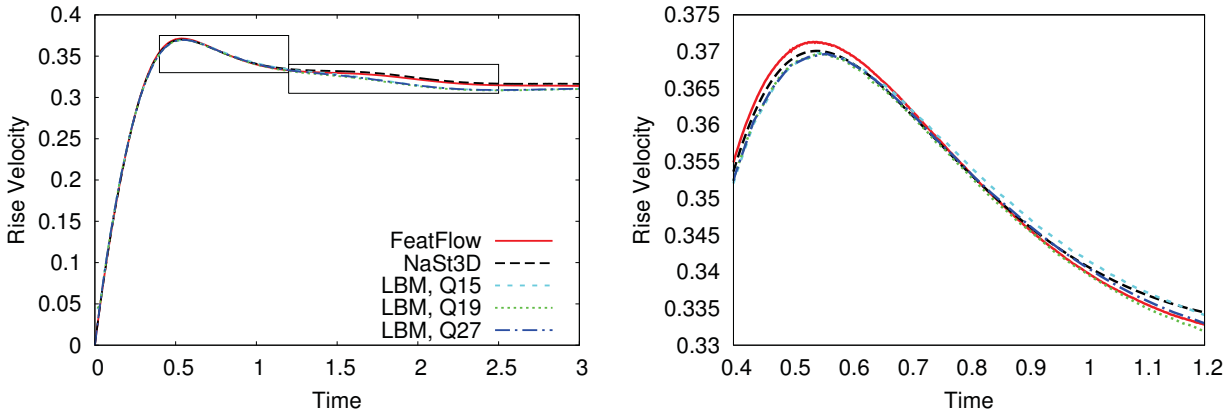

Fig. 18: Time evolution of rise velocity for 3D rising bubble TC2 (left), and enlarged views (right).

5 Numerical performance and stability in strong deformation singularities

After evaluating the accuracy of the 3D coupled scheme through benchmarking for rising bubbles, we may now proceed with simulations involving strong deformation singularities at high speeds so as to push the scheme towards its limits focusing more in the numerical stability and qualitative physical description. This includes the two problems of droplet splashing on a thin liquid film and the binary droplet collision. For this class of problems, a detailed quantitative comparison with other schemes and models is out of the scope of the current paper.

5.1 Droplet Splashing on thin liquid film

Splashing of a droplet over a thin liquid film is an attractive problem for both physicists and mathematicians. In fact, the resulting splashing patterns could vary significantly with the falling velocity and the density of the droplet. The different splashing regimes are classified using the Reynolds number Re as usual

$$Re = \frac{\rho_1 U_0 (2r_0)}{\mu_1}$$

together with the Weber number We

$$We = \frac{\rho_1 U_0 (2r_0)^2}{\sigma}$$

where U_0 is the velocity of the droplet at the impact moment. To show how critical the 3D simulations could be for this specific problem, we perform both 2D and 3D simulations using D2Q9 and D3Q19 lattice stencils, respectively. The 2D configuration used in [15] is adopted here, which is also extended to 3D simulations. It consists of a domain of size 2×1 where only half of the problem is considered and symmetry and periodic boundary conditions are used at $x = 0$ and $x = 2$ planes, respectively. The lower boundary is set to no-slip wall and a second order extrapolation is used to find the unknown distribution functions at the top boundary. A circular droplet with radius $r_0 = 0.25$ is initially located at $(x, y) = (0, 0.36)$, while the liquid film underneath has a depth of $H = 0.1$ as seen in figure 19.

In the following numerical experiments, the density and viscosity ratios are set to 1000 and 40, respectively and the surface tension forces are realized via $We = 8000$ for all cases. Figure 20 shows the temporal pattern of the splashing phenomenon on a lattice resolution of 256×512, where the time is measured based on $T = U_0 t_{lb}/(2r_0)$, with r_0 in lattice units. It can be seen that for $Re = 20$ which implies a small impact velocity, the droplet will be slowly deformed and flattened upon the film with no splashing effect developed. By increasing the Re number to 100 and 500, the splashing becomes fairly pronounced with a large rim and elevated fingers in the form of thin filaments.

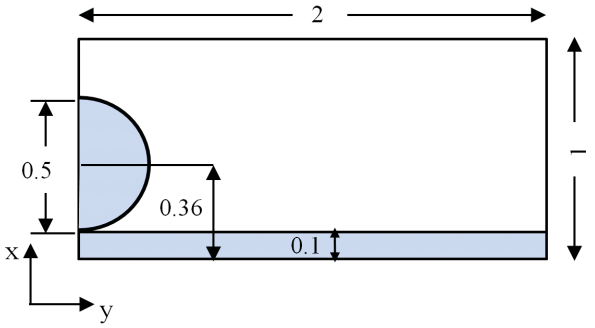

Fig. 19: Problem definition for the 2D droplet splashing on a thin liquid film.

The solution covers only 1/4 of the problem in 3D with symmetry boundary conditions on $x = 0$ and $y = 0$ planes, where the bubble hits the film along the z axis. The lattice resolution is $1/h = 128$, giving a domain size of $128 \times 256 \times 256$. Figures 21 and 22 show the 3D frames extended in the x direction. It could be seen that the edges of the ring become more straight while the ring itself attains a smaller radial extension as compared to the 2D case. Moreover, the spin-off of the satellite bubbles from the thinning rim for $Re = 500$ is more clearly captured and visible in 3D. Figure 23 presents a closer comparison between the 2D and 3D solutions on the cross section of the impact zone for different Re numbers. A major source of difference between the 2D and 3D cases is speculated to come from the increased surface tension effects in 3D which

try to resist against the velocity-driven deformations. From the energy point of view, the present 3D problem allows for the distribution of the initial impact kinetic energy of the droplet over a broader area, causing the effective impact zone to become relatively smaller than that of the 2D case.

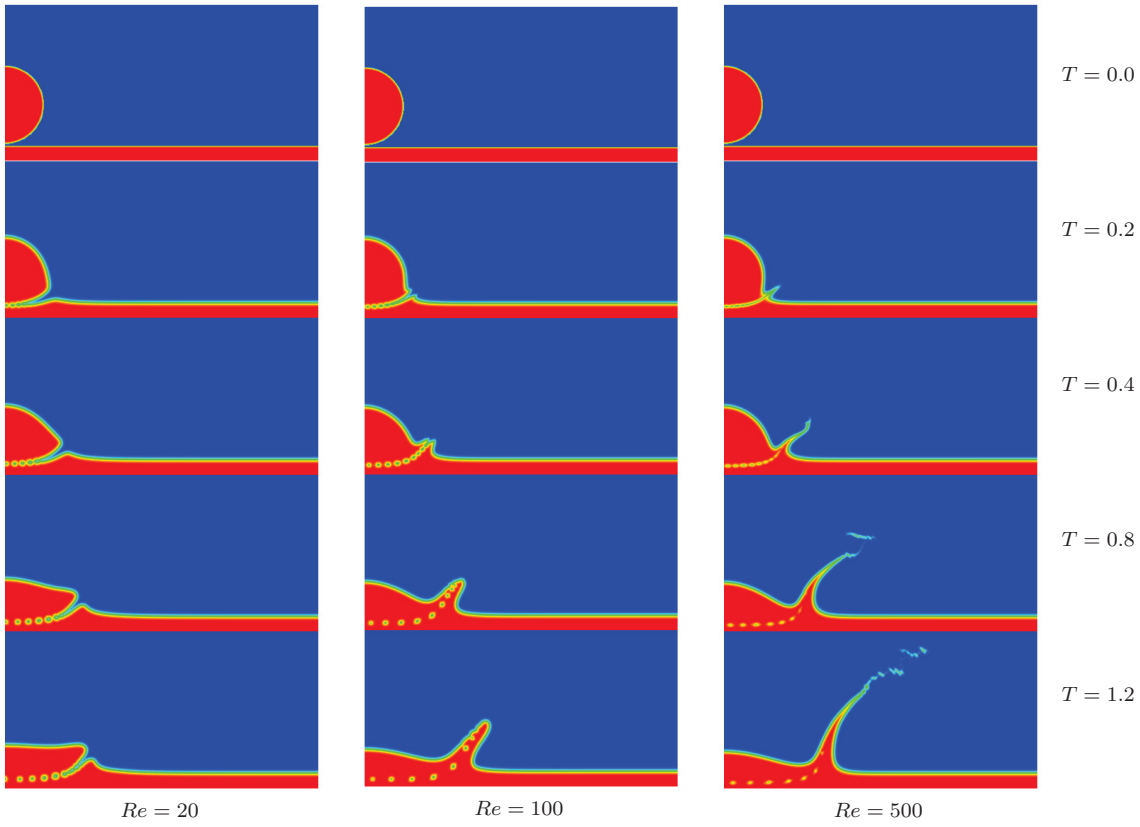

Fig. 20: Temporal evolution of the 2D droplet splashing over a thin film under different values of Re number.

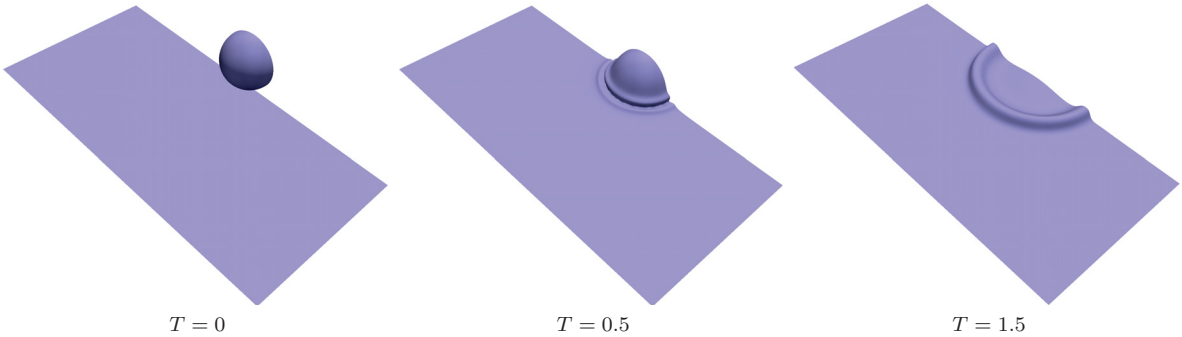

Fig. 21: Temporal evolution of the 3D droplet splashing over a thin film for $Re = 100$.

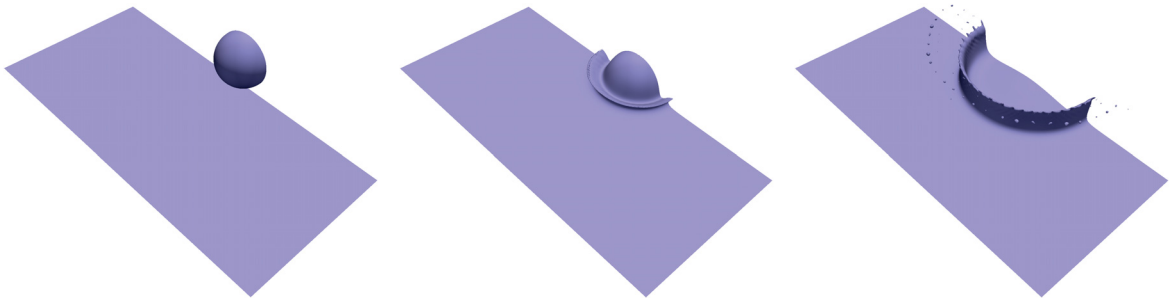

Fig. 22: Temporal evolution of the 3D droplet splashing over a thin film for $Re = 500$.

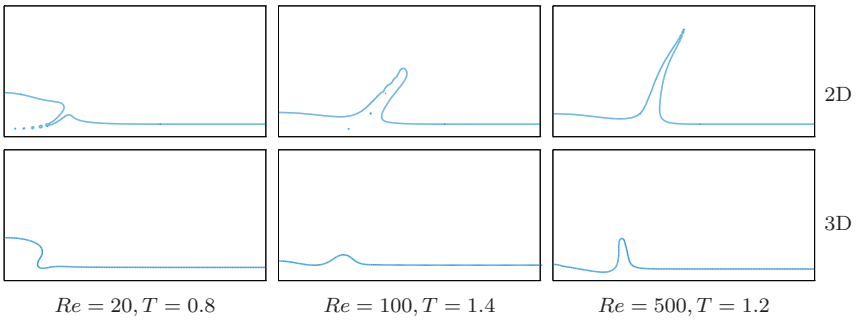

Fig. 23: Cross section of droplet impact zone in 2D (upper row) and 3D (lower row) problems.

5.2 Binary collision of droplets

The intriguing problem of binary droplet collision was first extensively studied in the experimental work of Ashghriz and Poo [4] where the evolution of the bubbles in different impact angles and arrangements was studied. Most importantly, they characterized the collisions using the Weber We and Reynolds Re numbers as in the case of droplet splashing, along with two additional parameters to specify the relative size and the impact angle of of the two droplets

$$\mathcal{D} = \frac{d_1}{d_2} \quad , \quad B = \frac{2X}{d_1 + d_2}$$

where d_1 and d_2 are the diameters of the two droplets and X is the distance between the center of one droplet to the relative velocity vector placed on the center of the other droplet [13]. In the present numerical experiments it is assumed that the droplets are of the same size, i. e., $\mathcal{D} = 1$ and $d_1 = d_2 = D$. The domain size is $3D \times 3D \times 6D$ and the droplets are initially placed $2D$ apart. The density and viscosity ratios are 1000 and 100, respectively, and the droplets collide with identical, but opposite velocities of $U_0/2$. Periodic boundary conditions are considered on all sides. For the case of a *head-on collision*, i. e., $B = 0$, the symmetry allows to solve for only 1/4 of the problem. As outlined in [4], for $500 < Re < 4000$ the Reynolds number has no significant role in the dynamics of the impact and it is thus fixed at $Re = 500$ such that the velocity magnitudes will remain in the low Ma regime on moderately fine lattices. The progress in time is measured in the units of U_0/D, with D in lattice units

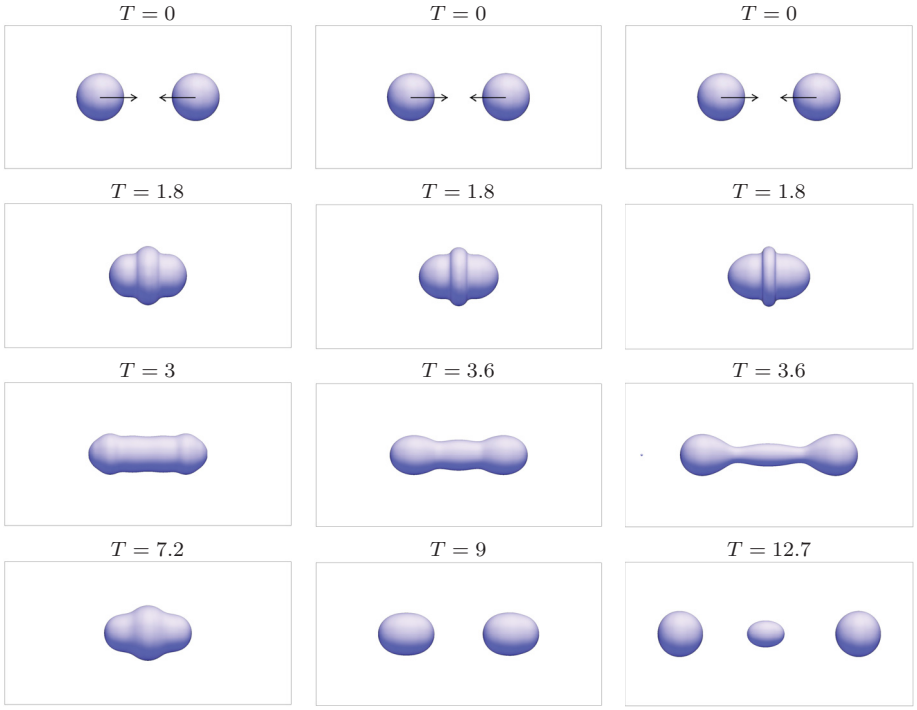

Fig. 24: Head-on collision of micro-droplets with $B = 0$, $Re = 500$ and (a) $We = 15$, (b) $We = 25$, (c) $We = 40$.

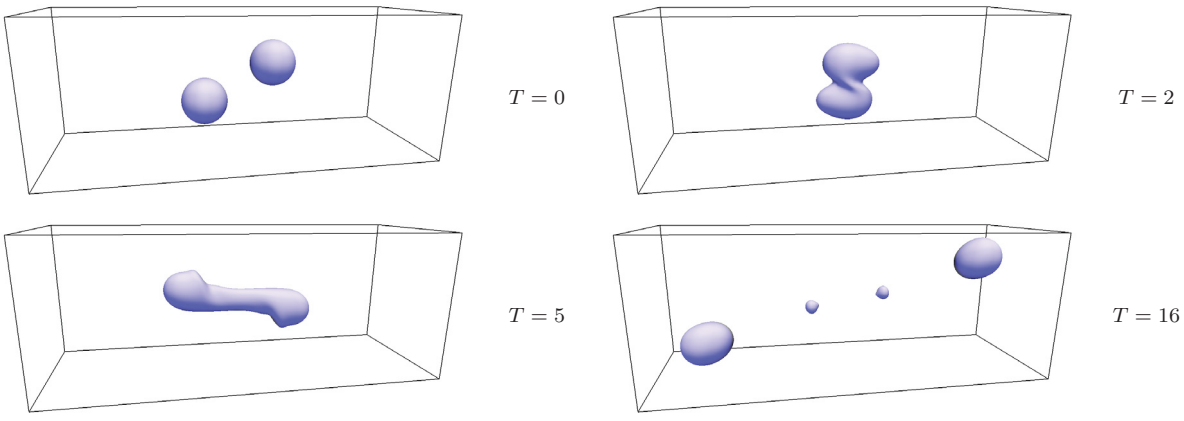

Fig. 25: Oblique collision of micro-droplets at $Re = 500$, $We = 80$ and $B = 0.8$.

Figure 24 shows the evolution of the colliding droplets for $We = 15, 25, 40$ on a domain size of $64 \times 64 \times 256$. The evolution of the droplets in all three cases shows a close agreement to the experimental data in [4]. For the high surface tension case of $We = 15$, the collision pattern falls into the *coalescence* regime, where the droplets merge and first form a circular disk. The disk then stretches out which is derived by the curvature

difference between its exterior and the interior. This initiates an oscillatory motion which eventually ends up in a larger circular droplet as $t \to \infty$. By increasing the Weber number to $We = 25$ the weaker surface tension allows for a thinner and larger disk in the middle, a stronger stretching and finally the spin-off of the merging droplets, after which, the droplets travel away from each other. This regime is therefore called *reflective separation*. By further increasing the Weber number to $We = 40$ the enhanced stretching causes the entire system to extend more such that the two round ends will no longer hold attached to the middle section and break-up, forming a third satellite bubble. The third bubble then remains in the middle and oscillates until becomes perfectly circular.

Figure 25 also shows the simulation result for the case of an oblique collision with $We = 80$ and $B = 0.8$. The droplets partially collide, but keep traveling close to their initial path. The oblique collision, however, causes a twist and rotary motion which creates a long connecting filament. The filament then separates from the main droplets and further breaks up into two satellite droplets. The obtained results for the head-on and oblique collisions closely repeat the patterns reported in [4]. Minor discrepancies, however, are expected since the boundary conditions and fluid properties might differ from those in real experiments and the LS method can not resolve the exact chemical potential field required to resolve the breakup regions.

6 Computational performance

Together with the general optimization rules instructed in [14, 19, 10, 27] for LB-based codes on GPGPUs, analysis of instruction and memory workload of the GPGPU parallel code implies a number of optimization measures as follows:

- Generate and use the directional forces on-the-fly and avoid saving and writing to and from the global memory.
- Limit the calculations for directional force as well as for $\mathbf{u} \cdot \nabla\psi$ to central type if $|\nabla\psi| < 10^{-9}$ for double precision (DP) and $|\nabla\psi| < 10^{-6}$ for single precision (SP) and hence avoid the large spatial support of upwind and WENO schemes far from the interface.
- In order to ease the instruction bottleneck caused by the matrix-vector operations, the MRT collision can be limited to $\psi > (1 - 10^{-9})$ and $\psi > (1 - 10^{-6})$ regions for DP and SP computations, respectively, thus leaving the rest of the domain to rely upon the low-cost SRT model.

The last two points comprise an adaptive computation refinement approach which comes as an effective tool in GPGPU implementations. Nevertheless, such an approach must be followed with care, as it depends on the specific dynamics of the problem under study.

Parallel computations are carried out on two high-end GPU-enabled compute machines. The first one is equipped with a Kepler K20Xm GPGPU, having a peak DP performances of 1.32 TFLOPS. For pure SP codes, a second machine equipped with GeForce GTX980 Ti gaming GPU with 5.6 TFLOPS in SP is employed. A comprehensive study on the errors associated with SP computations is done in [21], where the resulting maximum L_2 error in rising bubble quantities is reported to be $\approx 1\%$ for a lattice as fine as $1/h = 640$.

A summary of the simulation statistics using different stencils is presented in table 2 for the rising bubble TC1 until $T = 3$, where the total memory size occupied on GPGPU in GB is denoted by MGPU, number of time steps by NTS and the total simulation time in seconds by TGPU. Note that the simulation times also include the intermediate post-processing periods.

The performance of the 3D simulations in Million lattice update per second (MLUPS) for the D3Q19 stencil is given in figure 26. In order to compare the obtained performances with other two-LBE implementations on GPGPUs, we refer to the work of Banari et al. in [6] which uses SRT collisions for both flow and interface capturing LBEs and updates pressure via solving the pressure Poisson equation. Their DP computations on a Tesla C2070 GPGPU reached 20 MLUPS for D3Q19 simulations and large problem sizes. In comparison,

Table 2: Simulation statistics the 3D rising bubble using different lattice stencils

$1/h$	MGPU	NTS	TGPU	TGPU/NTS
		D3Q15		
96	0.17	26508	170	0.006
192	1.43	108300	4290	0.039
256	3.40	193548	17797	0.091
		D3Q19		
96	0.20	26508	207	0.007
192	1.65	108300	5329	0.049
256	3.93	193548	20774	0.107
		D3Q27		
96	0.26	26508	292	0.011
192	2.1	108300	7018	0.064
256	5.0	193548	29550	0.152

running the present codes in DP on Tesla C2070 device gives 30 MLUPS for the D3Q19 implementations and thus confirms at least 50% gain. In addition, the largest 3D problem in [6] occupied almost 6 GB of memory, whereas the present code needs only 1.9 GB to handle the same problem size.

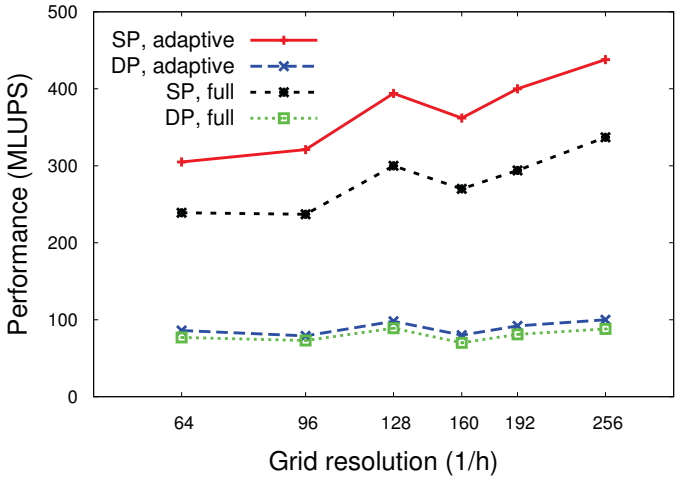

Fig. 26: Performance of the 3D coupled scheme using the D3Q19 velocity stencil.

7 Summary and conclusions

The coupled LB-level set two-phase method was utilized for the 3D benchmarking problems. Stability was improved through using MRT collision scheme and the LBE is coupled with a mass conserving interface capturing scheme. Compared to conventional two-LBE schemes the current method asks for considerably less amount of memory and gives 50% improvement in the computational performance. From the numerical point of view, the method appeared quite successful in both qualitative and quantitative aspects compared to the reference solutions. In particular, simulations for the high Eo number TC2 emphasize the fact that LB-based two phase flow solvers could reach the accuracy of sharp interface Navier-Stokes-based solution if the interface region is sufficiently refined. Since such coupled schemes do not need any iterative solver for the system of equations and could be efficiently parallelized, then employing higher resolutions than those

common in NSE solvers would certainly pay off in terms of memory and simulation time. Application of different discrete velocity models for the LBE revealed that the D3Q19 stencil provides the required isotropy at a reasonable extra cost compared to D3Q15, while the D3Q27 stencil asks for more than 50% longer simulation times and no noticeable accuracy improvement upon the D3Q19 stencil.

Acknowledgements

This work was supported by the German Graduate School of Energy Efficient Production and Logistics of the state of Nordrhein-Westfalen at TU Dortmund and by the DFG through the grant TU102/53 (SPP 1740).

References

[1] Featflow software, 2016. `http://www.featflow.de/en`.

[2] J Adelsberger, P. Esser, M. Griebel, S. Groß, M Klitz, and A. Rüttgers. 3d incompressible two-phase flow benchmark computations for rising droplets. pages 5274–5285, 2014.

[3] L. Amaya-Bower and T. Lee. Single bubble rising dynamics for moderate reynolds number using lattice boltzmann method. *Computers and Fluids*, 39(7):1191–1207, 2010.

[4] N. Ashgriz and J. Y. Poo. Coalescence and separation in binary collisions of liquid drops. *Journal of Fluid Mechanics*, 221:183–204, 12 1990.

[5] A. Banari, C. Janßen, S.T. Grilli, and M. Krafczyk. Efficient gpgpu implementation of a lattice boltzmann model for multiphase flows with high density ratios. *Computers and Fluids*, 93:1–17, 2014.

[6] A. Banari, C.F. Janßen, and S.T. Grilli. An efficient lattice boltzmann multiphase model for 3d flows with large density ratios at high reynolds numbers. *Computers and Mathematics with Applications*, 68(12):1819–1843, 2014.

[7] M. Cheng, J. Hua, and J. Lou. Simulation of bubble-bubble interaction using a lattice boltzmann method. *Computers and Fluids*, 39(2):260–270, 2010.

[8] Grace J. R. Clift, R. and M. E. Weber. *Bubbles, Drops and Particles*. Academic Press, New York, First edition, 1978.

[9] D. D'Humières, I. Ginzburg, M. Krafczyk, P. Lallemand, and L.-S. Luo. Multiple-relaxation-time lattice boltzmann models in three dimensions. *Philosophical Transactions of the Royal Society A: Mathematical, Physical and Engineering Sciences*, 360(1792):437–451, 2002.

[10] M. Geveler, D. Ribbrock, D. Göddeke, and S. Turek. Lattice-boltzmann simulation of the shallow-water equations with fluid-structure interaction on multi- and manycore processors. *Lecture Notes in Computer Science (including subseries Lecture Notes in Artificial Intelligence and Lecture Notes in Bioinformatics)*, 6310 LNCS:92–104, 2010.

[11] X. He, X. Shan, and G.D. Doolen. Discrete boltzmann equation model for nonideal gases. *Physical Review E - Statistical Physics, Plasmas, Fluids, and Related Interdisciplinary Topics*, 57(1):R13–R16, 1998.

[12] S. Hysing, S. Turek, D. Kuzmin, N. Parolini, E. Burman, S. Ganesan, and L. Tobiska. Quantitative benchmark computations of two-dimensional bubble dynamics. *International Journal for Numerical Methods in Fluids*, 60(11):1259–1288, 2009.

[13] T. Inamuro, T. Ogata, S. Tajima, and N. Konishi. A lattice boltzmann method for incompressible two-phase flows with large density differences. *Journal of Computational Physics*, 198(2):628–644, 2004.

[14] F. Kuznik, C. Obrecht, G. Rusaouen, and J.-J. Roux. Lbm based flow simulation using gpu computing processor. *Computers and Mathematics with Applications*, 59(7):2380–2392, 2010.

[15] T. Lee and C.-L. Lin. A stable discretization of the lattice boltzmann equation for simulation of incompressible two-phase flows at high density ratio. *Journal of Computational Physics*, 206(1):16–47, 2005.

[16] T. Lee and L. Liu. Lattice boltzmann simulations of micron-scale drop impact on dry surfaces. *Journal of Computational Physics*, 229(20):8045–8063, 2010.

[17] M. Mehravaran and S. Kazemzadeh Hannani. Simulation of buoyant bubble motion in viscous flows employing lattice boltzmann and level set methods. *Scientia Iranica*, 18(2):231 – 240, 2011.

[18] S. Mukherjee and J. Abraham. A pressure-evolution-based multi-relaxation-time high-density-ratio two-phase lattice-boltzmann model. *Computers and Fluids*, 36(6):1149–1158, 2007.

[19] C. Obrecht, F. Kuznik, B. Tourancheau, and J.-J. Roux. A new approach to the lattice boltzmann method for graphics processing units. *Computers and Mathematics with Applications*, 61(12):3628–3638, 2011.

[20] E. Olsson and G. Kreiss. A conservative level set method for two phase flow. *Journal of Computational Physics*, 210(1):225–246, 2005.

[21] M. A. Safi. *Efficient computations for multiphase flow problems using coupled lattice Boltzmann-level set methods*. PhD thesis, Fakultät für Mathematik, Technischen Universität Dortmund, 2016. `https://eldorado.tu-dortmund.de/handle/2003/35115`.

[22] M.A. Safi and S. Turek. Efficient computations for high density ratio rising bubble flows using a diffused interface, coupled lattice boltzmann-level set scheme. *Computers and Mathematics with Applications*, 70(6):1290–1305, 2015.

[23] M.A. Safi and S. Turek. Gpgpu-based rising bubble simulations using a mrt lattice boltzmann method coupled with level set interface capturing. *Computers and Fluids*, 124:170–184, 2016.

[24] K. Suga, Y. Kuwata, K. Takashima, and R. Chikasue. A d3q27 multiple-relaxation-time lattice boltzmann method for turbulent flows. *Computers and Mathematics with Applications*, 69(6):518–529, 2015.

[25] M. Sussman and E. Fatemi. Efficient, interface-preserving level set redistancing algorithm and its application to interfacial incompressible fluid flow. *SIAM Journal on Scientific Computing*, 20(4):1165–1191, 1999.

[26] N. Takada, M. Misawa, A. Tomiyama, and S. Fujiwara. Numerical simulation of two- and three-dimensional two-phase fluid motion by lattice boltzmann method. *Computer Physics Communications*, 129(1):233–246, 2000.

[27] J. Tolke and M. Krafczyk. Teraflop computing on a desktop pc with gpus for 3d cfd. *Int. J. Comput. Fluid Dyn.*, 22(7):443–456, 2008.

[28] S. Turek, O. Mierka, S. Hysing, and D. Kuzmin. Numerical study of a high order 3D FEM–level set approach for immiscible flow simulation. In S. Repin, T. Tiihonen, and T. Tuovinen, editors, *Numerical methods for differential equations, optimization, and technological problems*, Computational Methods in Applied Sciences, Vol. 27, pages 65–70. Springer, 2012.

[29] Hakon Wadell. Volume, shape, and roundness of quartz particles. *The Journal of Geology*, 43(3):pp. 250–280, 1935.

[30] D. Zhang, K. Papadikis, and S. Gu. Three-dimensional multi-relaxation time lattice-boltzmann model for the drop impact on a dry surface at large density ratio. *International Journal of Multiphase Flow*, 64:11–18, 2014.

[31] H.W. Zheng, C. Shu, and Y.T. Chew. A lattice boltzmann model for multiphase flows with large density ratio. *Journal of Computational Physics*, 218(1):353–371, 2006.